

Robust transverse structures in rescattered photoelectron wavepackets and their observable consequences

Timm Bredtmann^{1,*} and Serguei Patchkovskii¹

¹*Max-Born-Institute, Max-Born-Straße 2A, D-12489 Berlin, Germany*

Abstract

Initial-state symmetry has been underappreciated in strong-field spectroscopies, where laser fields dominate the dynamics. We demonstrate numerically that the transverse photoelectron phase structure, arising from this symmetry, is robust in strong-field rescattering, and manifests in strong-field photoelectron spectra. Interpretation of rescattering experiments need to take these symmetry effects into account. In turn, transverse photoelectron phase structures may enable attosecond super-resolution imaging with structured electron beams.

arXiv:1810.12672v2 [physics.atom-ph] 20 May 2019

* Timm.Bredtmann@mbi-berlin.de

Symmetries, exact and approximate, and symmetry breaking underpin our understanding of perturbative spectroscopies [1, 2], where field-free symmetries of initial and final states constrain the range of outcomes. In contrast, in intense infrared laser fields, the dynamics are dominated by the field itself. For example, strong infrared pulses can remove an electron from an atom, a molecule or in a solid (ionization), accelerate it (propagation), and finally drive it into the parent ion (recollision). This is the three-step model [3, 4], capturing the essence of the emerging field of attosecond (asec) strong-field spectroscopies [5–7]. In the recollision step the returning electronic wavepacket (REWP) may recombine to the parent-ion, giving rise to high-harmonics generation [5–10], or scatter elastically, yielding strong-field photoelectron holography [11–13] and laser-induced electron diffraction (LIED) [5, 6, 10, 13–23].

The symmetry of the laser field, and the dynamical symmetry it imposes on the continuum wavepacket, determine many qualitative features of these processes by means of selection rules [24]. It is widely recognized that tunnel-ionized electrons that do not recollide give information about the initial-state symmetry [13, 17]. At higher energies, holographic patterns are sensitive to the phase-structure of the REWP [12], which may arise from the asymmetry in the binding-potential [12] or the initial-state symmetry [13]. However, in other strong-field spectroscopies such as LIED it is commonly assumed that the laser field entirely dominates subsequent dynamics, and the transverse phase structure due to the initial-state symmetry is “washed” out in the propagation step [10], yielding an asymptotically-flat wavefront. This assumption is implicitly enforced by the stationary-phase treatment of the strong-field approximation (SFA) [8, 9].

Recently, an experimental/theoretical study in our institute [25] has shown that the rescattering probability in trans-butadiene is specific to the ionization channel and the molecular orientation, rather than a property of the driving field alone. These results imply that the REWP may retain, despite the strong driving field, the transverse phase structure imprinted by the initial state. Such structure will significantly influence the recollision process and alter the shape and the interpretation of strong-field photoelectron spectra. Ultimately it may enable atomic-scale engineering of structured electron beams – an electron-beam analogue to structuring the illumination in super-resolution light microscopy [26].

Unfortunately, limited statistics [25] precluded measuring the angle- and ionization-channel-resolved photoelectron spectra, permitting alternative interpretations. The goal of

this Letter is to numerically explore the consequences of the initial-state symmetry for the LIED region of strong-field photoelectron spectra. We are particularly interested in determining whether these effects are robust to the misalignment between the field-free symmetry elements and the laser-field polarization.

In molecular systems, the initial-state symmetry effects are intertwined with contributions due to the potential asymmetry [12], orientation, and nuclear motion. Combined with the cost of solving the time-dependent Schrödinger equation (TDSE), this complexity makes a conclusive analysis challenging. Instead, we consider the simplest-possible example of the initial-state symmetry: a one-electron atom (He^+ or “Argon” [27]), initially in an antisymmetric p state. We solve the three-dimensional TDSE in the velocity gauge and dipole approximation [27, 28]. The simulation grid contains 2200 radial points with spacings of $\Delta r = 0.2 a_0$, and angular momentum channels up to $L \leq 40$, $|M| \leq 40$. The time-step is $\Delta t = 0.03$ asec and a transmission-free absorbing potential [29] is applied at $r = 407.6 a_0$. The photoelectron spectra are calculated using surface-flux integration [30, 31] continued to infinite time [27]. Sine-squared envelopes are used for the vector potential $A(t)$, with carrier-envelope phase of $\pi/2$ (corresponding to the time-odd electric field $E(t) = -\partial A(t)/\partial t$).

Figure 1(a) shows strong-field photoelectron spectra for the He^+ ion. The 5 cycle, 800 nm electric field with peak intensity $I_{\text{max}} = 10^{14}$ W/cm² is linearly-polarized along the z direction. At first, we explore two initial states $|\Psi_0\rangle$: symmetric ($|\Psi_0\rangle = |2p_z\rangle$, left column) and anti-symmetric ($|\Psi_0\rangle = |2p_x\rangle$, right column) with respect to the σ_{yz} -reflection. The vertical axis (k_{\parallel}) coincides with the laser polarization direction and the horizontal axis (k_{\perp}) with the “averaged” perpendicular direction. The averaging of the strong-field photoelectron spectra is performed in spherical coordinates over the azimuthal angle ϕ , separately in the “left” and “right” hemispheres. Hence, the “left” side of the spectra ($k_{\perp} < 0$) average over $90^\circ < \phi < 270^\circ$; the “right” side ($k_{\perp} > 0$) over $\phi < 90^\circ$ and $\phi > 270^\circ$. Finally, the polar angle θ is defined with respect to the laser polarization direction (k_{\parallel} -axis).

For the symmetric $2p_z$ case (left panel), we observe a typical strong-field photoelectron spectrum symmetric with respect to perpendicular momenta k_{\perp} , including holographic “fingers” in the lower-energy region below $2U_p$ (U_p is the ponderomotive energy) [11–13] and recollision circles for back-scattered electrons [10] (small deflection angles θ_r in our notation). The $10U_p$ ($6U_p$) recollision circles and the definition of the deflection angle θ_r are indicated by the yellow (black) lines. The $10U_p$ circles correspond to electrons that return with maxi-

mal kinetic energy to the ion core, elastically backscatter ($|\theta_r| < 90^\circ$), and gain an additional drift momentum equal to the vector potential at the moment of recollision $A(t_r)$ [10]. The maximal energy gain corresponds to $\theta_r = 0^\circ$. This definition of the deflection angle is chosen to simplify the discussion of orientational averaging below. It differs from the conventional electron-diffraction definition [10] by 180° . For the anti-symmetric $2p_x$ case (right panel), i.e. polarization of the laser field within the symmetry plane, the photoelectron spectra change dramatically, now vanishing for $k_\perp = 0$ ($\theta_r = 0^\circ$).

The corresponding angle-resolved spectrum along the $10U_p$ ($6U_p$) circle is shown in the left (right) panel of Fig. 1(b) (solid lines). Dashed lines give the focal-spot average (see appendix for details, including the full angle-resolved 2D maps in Fig. S5). For the symmetric case ($|2p_z\rangle$, green line), the yield along the $10U_p$ circle largely follows the Rutherford scattering cross-section, allowing retrieval of structural information in LIED [10]. For the anti-symmetric case ($|2p_x\rangle$, blue line), the yield for the perfect back-scattering ($\theta_r = 0^\circ$) vanishes and its angular dependence is changed qualitatively. Focal averaging does not significantly affect these results. The $6U_p$ circle (right) shows the same characteristic difference between the symmetric (green) and anti-symmetric (blue) case, although the detailed structure is complicated due to intensity-dependent interferences with late electron returns [5, 32]. These interferences lead e.g. to a maximum at $\theta_r = 0^\circ$ for the anti-symmetric case (blue solid line) and are largely suppressed by focal averaging (dashed lines).

These results agree with the SFA rescattered-photoelectron amplitude [33]:

$$a(\mathbf{k}_f) = - \int dt_0 dt_c d\mathbf{p} e^{-iS_V(t_0, t_c, \mathbf{p})} \times R \times I, \quad (1)$$

where the elastic scattering and photoionization matrix elements are:

$$R = \langle \mathbf{k}_f + A_z(t_c) | V_c | \mathbf{p} + \hat{\mathbf{z}} A_z(t_c) \rangle,$$

$$I = \langle \mathbf{p} + A_z(t_0) | V_L(t_0) | \Psi_0 \rangle.$$

Integration in Eq. (1) is over the ionization and recollision-times t_0 and t_c , respectively, and the canonical momentum \mathbf{p} . The quantity $S_V(t_0, t_c, \mathbf{p})$ is the length-gauge Volkov phase [9] and $\hat{\mathbf{z}} A_z(\tau)$ the vector potential ($\hat{\mathbf{z}}$ is the unit vector in z direction). Finally, V_c is the Coulomb potential, $V_L(t_0) = z E_z(t_0)$ describes the interaction of the z -polarized laser field $E_z(t_0)$ and the atom, and $|\Psi_0\rangle$ is the initial state.

In the lowest-order stationary-phase approximation (SPA) Eq. (1) becomes [33]:

$$a(\mathbf{k}_f) \propto e^{-iS_V(t_{0s}, t_{cs}, \mathbf{p}_s)} \times R_s \times I_s, \quad (2)$$

with the stationary matrix elements

$$\begin{aligned} R_s &= \langle \mathbf{k}_f + A_z(t_{cs}) | V_c | \hat{\mathbf{z}}(p_{sz} + A_z(t_{cs})) \rangle \\ I_s &= \langle \hat{\mathbf{z}}(p_{sz} + A_z(t_{0s})) | V_L(t_{0s}) | \Psi_0 \rangle, \end{aligned}$$

where t_{0s}, t_{cs} and \mathbf{p}_s are the stationary points of the Volkov phase. The perpendicular component of the stationary canonical momentum $p_{s\perp}$ vanishes [9, 33].

For the symmetric $2p_z$ case, R_s is the Rutherford scattering cross-section [10] and the recollision is described by a single trajectory with zero transverse momentum (Fig. 1(a), upper-left panel). For the anti-symmetric $|2p_x\rangle$ initial state the stationary hydrogenic photoionization matrix element:

$$I_s \propto \frac{(p_{sz} + A_z(t_{0s}))p_{sx}}{(4(p_{sz} + A_z(t_{0s}))^2 + 4)^4}$$

vanishes by symmetry ($p_{sx} = 0$). The lowest-order SPA rescattered amplitude then vanishes [34], and higher orders must be considered in evaluating Eq. (1). Expanding the matrix elements I and R in Eq. (1) in the transverse component of the canonical momentum \mathbf{p} around the stationary point \mathbf{p}_s , we obtain, in the lowest surviving order [25]:

$$\begin{aligned} a(\mathbf{k}_f) &\propto e^{-iS_V(t_{0s}, t_{cs}, \mathbf{p}_s)} \left(\frac{1}{i(t_{cs} - t_{0s})} \right) \times \tilde{R}_s \times \tilde{I}_s \quad (3) \\ \tilde{I}_s &= \left. \frac{\partial}{\partial p_x} \langle \mathbf{p} + A_z(t_0) | V_L(t_0) | 2p_x \rangle \right|_{\mathbf{p}=p_{sz}} \\ \tilde{R}_s &= \left. \frac{\partial}{\partial p_x} \langle \mathbf{k}_f + A_z(t_c) | V_c | \mathbf{p} + A_z(t_c) \rangle \right|_{\mathbf{p}=p_{sz}}. \end{aligned}$$

For a hydrogenic state:

$$\begin{aligned} \tilde{I}_s &\propto \frac{(p_{sz} + A_z(t_{0s}))}{(4(p_{sz} + A_z(t_{0s}))^2 + 4)^4} \\ \tilde{R}_s &\propto \frac{k_{fx}}{(|\mathbf{k}_f - p_{sz}|^2)^2}. \end{aligned}$$

Thus, for laser polarization along a symmetry plane, the REWP can no longer be described by an asymptotically-flat wavefront with a well-defined return direction along the

laser polarization. Instead, we can introduce an (arbitrary) small transverse momentum Δp_{sx} . For an atomic $2p_x$ initial state, the finite-difference expression for \tilde{I}_s and \tilde{R}_s then factorizes into a sum of two contributions (or trajectories) with π phase difference, added coherently (Fig. 1(a), top right). Their interference alters the high-energy (LIED) region of the photoelectron spectrum, in particular suppressing the signal for $k_{fx} = 0$.

In order to explore the robustness of our results with respect to misalignment of the laser-polarization direction and the symmetry plane of the initial state, Figure 2(a) shows the photoelectron spectrum for a misalignment angle of $\alpha = 10^\circ$. The same z polarized pulse as in Fig. 1(a) with single peak intensity $I_{\max} = 10^{14}$ W/cm² is used. Moreover, Fig. 2(b) shows the corresponding focal-averaged spectrum with the same peak intensity. Both in the single-intensity and in the focal-averaged photoelectron spectrum the signatures of the phase structure of the REWP are quite different in the lower-energy (holographic) and the higher-energy (LIED) region: In the holographic region, the photoelectron signal is suppressed close to $k_\perp = 0$, clearly reflecting the symmetry plane of the initial state [13]. This behaviour is qualitatively similar to exact laser polarization along a symmetry plane ($\alpha = 0^\circ$) (Fig. 1(a), right panel). As expected, a “left”–“right” asymmetry of the photoelectron signal is present for $\alpha = 10^\circ$, which breaks the overall reflection symmetry.

In the LIED region effects of the initial-state symmetry are more subtle for $\alpha = 10^\circ$. Here, the non-symmetric initial state gives rise to a transverse phase gradient of the REWP. This phase gradient results in a left–right asymmetry, and the corresponding displacement of the minimum along the recollision circles. This behaviour is illustrated further in Fig. 2(c) which shows the angle-resolved photoelectron yield for the single-intensity case (Fig. 2(a)) along the same recollision-circles used in Fig. 1 as function of the misalignment angle α . For the $10U_p$ circle (left panel), the white line traces the photoelectron minimum for each α . For $\alpha = 10^\circ$ the minimum lies around $\theta_r = -13^\circ$. This displacement deviates considerably from the Rutherford scattering cross section with minimum at $\theta_r = 0^\circ$ (Fig. 1(b), left panel). This behaviour corresponds to counter-rotation of the photoelectron signal with the initial state which prevails well beyond $\alpha = 20^\circ$ (results are shown up to $\alpha = 20^\circ$). The counter-rotation is even more pronounced along the $6U_p$ recollision circle (Fig. 2(c), right panel). This left–right asymmetry can be understood as the interference of the signals from equations (2) and

(3), sketched in Fig. 1(a). With $|\Psi_0\rangle = \sin(\alpha)|2p_z\rangle + \cos(\alpha)|2p_x\rangle$, we get:

$$a(\mathbf{k}_f) \propto e^{-iS_V(t_{0s}, t_{cs}, \mathbf{p}_s)} \times \left(\sin(\alpha) R_s \times I_s + \cos(\alpha) \left(\frac{1}{i(t_{cs} - t_{0s})} \right) \tilde{R}_s \times \tilde{I}_s \right). \quad (4)$$

(In the holographic region, an additional interference with the direct-electron “reference” wave will also be present.) Hence, also for an imperfect alignment the photoelectron phase structure clearly influences the recollision process both in the holographic and LIED region. These results are robust with respect to focal averaging (see Figure S5).

Finally, Figure 3(a) shows the photoelectron spectrum for an “Argon” atom interacting with the same single-intensity laser field used in Figs. 1 and 2. For laser polarization exactly along a symmetry plane ($|3p_x\rangle$; left panel), results are similar to the He^+ ion (cf. Fig. 1(a), right). In particular, the photoelectron signal vanishes for $k_\perp = 0$ due to the symmetry plane of the initial state, both in the holographic and the LIED regions. For $\alpha = 10^\circ$ (right panel), significant differences between the argon atom and the He^+ ion occur: In the holographic region, the photoelectron spectrum co-rotates with the initial state for the argon atom, whereas it is strongly suppressed around $k_\perp = 0$ for the He^+ ion (Fig. 2(a)).

In the LIED region the symmetry-induced phase structure of the REWP also results in co-rotation of the signal for $\alpha \neq 0^\circ$, and the corresponding shift of the minima along the recollision circles. For the $10U_p$ circle (Fig. 3(b), left), white lines trace the photoelectron minima for each α . For $\alpha = 10^\circ$, the minima along θ_r are shifted by $\approx 4^\circ$ relative to the symmetric case ($\alpha = 90^\circ$). As for the He^+ ions, the left–right asymmetry is more pronounced along the $6U_p$ recollision circle (Fig. 3(b), right). However, we observe a co-rotation of the photoelectron signal with the initial state, whereas the signal counter-rotates with the initial state for the He^+ -ion (Fig. 2(c)), illustrating the sensitivity of the phase structure of the REWP on the specific quantum system.

In summary, we demonstrate that the initial-state symmetry imposes a phase structure on the recolliding electron wavepacket, which modifies strong-field rescattering. Thus, the complete characterization of the rescattered photoelectron may be possible not only in the holographic [12], but also in the background-free high-energy rescattering region of the strong-field photoelectron spectrum. The signatures of the photoelectron’s phase structure, especially of its transverse phase gradient, are robust in the strong-field spectra to field misalignment with respect to the symmetry plane and depend sensitively on the quantum system (Figs. 2 and 3). Moreover, these signatures are robust with respect to focal averaging

(Figs. 1(b) and 2(b)) and with respect to the peak laser intensity (appendix). Hence, initial-state symmetry needs to be accounted for in the interpretation of strong-field recollision experiments both in the lower-energy (holographic) and the higher-energy (LIED) region. The numerical results are supported by an analytical model based on an extension of the standard stationary-phase approximation of the rescattered-electron SFA [8, 9, 25]. While we concentrate on the holographic and the LIED regions, we expect that other features of strong-field photoelectron spectra such as interference carpets [35] may be affected as well.

The symmetry-induced continuum phase structures are expected to be important for complex molecular systems as well, by interchanging the structural minima and maxima in laser-induced diffraction (see [36] for a similar effect in high harmonics generation and the appendix). While strong-field ionization along a nodal plane may be suppressed in small molecules [37], this constraint is relaxed for a broad range of typical organic molecules [25, 38], where coincidence measurements may be used to disentangle contributions from different ionization channels [25].

In turn, robust transverse phase structure of the returning wavepacket is the prerequisite for attosecond super-resolution imaging with structured electron beams. For example, initial states carrying ring-currents [39, 40] would lead to atomic-scale electronic vortex (doughnut) beams, analogous to light vortices used in super-resolution light microscopy [26]. Such structured attosecond electron beams may specifically probe certain regions within a molecule and thereby enhance the spatial resolution. While the detailed investigation of nano-structured electron beams will be presented elsewhere [41], the appendix gives illustrative examples. We show how the phase structure of such beams, coming from the initial p_{\pm} , d_{\pm} , and real-valued d states, are mapped, background-free, onto the angle-resolved rescattering spectra (Figs. S1, S2). In molecules, the transverse phase gradient of the nano-structured returning electron beam is expected to enhance interferences between individual scattering centers (atoms), resolving structural features well-below the usual de Broglie limit (Figs. S3, S4). Conversely, a known molecular structure can also be used to characterize the phase structure of the returning electronic wavepacket.

ACKNOWLEDGMENTS

We thank Jens Biegert, Jochen Mikosch, and Michael Spanner for inspiring discussions and helpful advice.

Appendix A: Initial-state symmetries

Figure S1 adds ring-current carrying states to the discussed initial-state symmetries, see rightmost panels. For comparison to the main text, the left panels of Fig. S1 show the corresponding strong-field photoelectron spectra for the symmetric initial $2p_z$ state and the middle panels for the anti-symmetric initial $2p_x$ state already discussed in Figure 1 in the main text. Here we visualize the three-dimensional photoelectron spectrum by means of isosurfaces (Fig. S1(a)), and by two-dimensional cuts perpendicular to the laser-polarization direction (z -direction, Fig. S1(b)). We nicely see how the initial-state symmetries are mapped to the strong-field photoelectron spectrum. In particular, current-carrying initial states give rise to electronic vortex (doughnut) beams with intensity minimum in the center of the beam, which is mapped to the photoelectron spectrum. Figure S2(b) shows the corresponding two-dimensional cuts for initial ring-current carrying $3d_{\pm 1}$ (top) and $3d_{\pm 2}$ states (bottom). Light vortices are used in super-resolution light microscopy, see Ref. [26] in the main text. Here, we demonstrate atomic-scale electronic vortex beams, which may enhance the resolution in strong-field spectroscopies, giving rise to attosecond, sub-Ångström super-resolution spectroscopy.

Moreover, the high-energy rescattering region of the strong-field photoelectron spectra carries background-free imprints of the initial-state symmetry in the planes transverse to the laser polarization direction, see Figs. S1 and S2. Part (a) of the latter Figure shows the corresponding planes for the five real d-orbitals (from top to bottom) $3d_{z^2}$, $3d_{x^2-y^2}$, $3d_{xy}$, $3d_{yz}$, $3d_{zx}$ as initial states.

Appendix B: Transverse structures of rescattered photoelectrons in molecules

Implications and opportunities of transverse structures of rescattered photoelectrons in molecules may be illustrated by means of a double-slit *Gedankenexperiment*. For simplicity, we consider the two-dimensional case, where a monochromatic plane wave, with wavevector

$k = 2\pi/\lambda$, illuminates two narrow slits separated by a distance d at normal incidence. Figure S3(a) shows the corresponding far-field diffraction pattern, $I(\theta) \propto \cos(\pi\frac{d}{\lambda}\sin(\theta))^2$, as function of the diffraction angle θ for $\frac{d}{\lambda} = 2$. The characteristic diffraction minima allow a straightforward determination of the slit separation d .

Figure S3(b) shows the analogous case for an incoming wave with $\Phi = \pi$ phase jump between the slits, giving rise to the far-field diffraction pattern $I(\theta) \propto \cos(\pi\frac{d}{\lambda}\sin(\theta) + \frac{1}{2}\Phi)^2$. This case corresponds to strong-field ionization and rescattering along a nodal plane as demonstrated in the main text. In particular, the returning electronic wavepacket can no longer be described by an asymptotically-flat wavefront with well-defined return direction with respect to the laser polarization direction, as is typically done in state-of-the-art LIED experiments, see e.g. Refs. [13,18-23] in the main text. Instead, the returning electronic wavepacket may be approximated by two trajectories with π phase difference, see Fig. 1(a) (right panel) and discussion following eqn. (3) in the main text. This scenario translates directly to molecules due to the underlying symmetry.

Finally, Figure S3(c) shows the diffraction pattern for a phase difference of $\Phi = \pi/2$ between the two emitters. This case corresponds to imperfect alignment between the laser polarization axis and the symmetry element of the initial state, demonstrated in the main text, see Figures 2 and 3. Here, the returning electronic wavepacket is composed of different return directions which need to be added coherently, see eqn. (4) in the main text. Also, these return directions depend sensitively on the specific quantum system as shown in the main text, c.f. Figs. 2 and 3.

The demonstrated robust transverse phase structures of the rescattered photoelectron are not only crucial in the interpretation of state-of-the-art strong-field rescattering experiments but also present opportunities for strong-field imaging. Figure S4 illustrates, in addition to attosecond vortex beams (Appendix A), another way of how these transverse structures may enable super-resolution strong-field imaging. Again we stress that, while the main text treated atoms, such transverse structures of rescattered photoelectrons will also be present in molecular systems due to the underlying symmetry, see also Refs. [12,25]. Specifically, analogous to super-resolution light microscopy (Ref. [26]), structured rescattered photoelectrons may enable structure determination beyond the diffraction limit. Figure S4(a) shows the standard far-field double-slit diffraction pattern far beyond the diffraction limit for a ratio $d/\lambda = 0.1$. Besides the absence of diffraction minima, the overall diffraction pattern is

rather unstructured, rendering structural determination with realistic signal-to-noise ratios practically impossible. The same is true for $\Phi = \pi$ (Figure S4(b)), i.e. a π phase shift between the emitters. On the other hand, for $\Phi = \pi/2$ (Figure S4(c)) the pattern is much more structured, which is most apparent close to the backscattering region around $\theta = 180^\circ$ crucial to strong field imaging, Refs. [5,6,10,13-23] in the main text. Specifically, the slope of the diffraction pattern in the backscattering region is related to the slit separation d through $I'(\theta = 0) \propto -\cos(\frac{1}{2}\Phi)\sin(\frac{1}{2}\Phi)\frac{d}{\lambda}$. Hence, with known phase difference Φ between the emitters, the determination of the slit separation d becomes in principle possible, even much beyond the diffraction limit. On the other hand, a known slit separation (known inter-nuclear distance) allows the determination of the phase-gradient of the returning electronic wavepacket.

Also, detailed analysis of the tilt of the diffraction pattern as function of the misalignment angle between the laser polarisation and initial state symmetry elements (see Figures 2(c) and 3(b) in the main text) may enable the determination of the phase structure of the recolliding electronic wavepacket. The corresponding shift of the holographic fringes may equally aid in the characterisation of the structure of the continuum wavepacket, see also Ref. [12].

Appendix C: Focal averaging

Figure S5 explores the effect of focal averaging for the He^+ atom. We assume a Gaussian beam for which the volume of the focal spot is given by:

$$\begin{aligned}
 V &= V_0(y^3 + 6(y - \text{atan}(y))) && \text{with} \\
 V_0 &= (2\pi/9)w_0^2 * Z_r && \text{and} \\
 y &= \sqrt{I_{\text{max}}/I_0 - 1}
 \end{aligned}$$

where I_{max} is the peak intensity, w_0 is the beam waist, and Z_r is the Rayleigh range. Because we are not interested in the absolute numbers, we set V_0 to 1 from now on.

Figure S5(a) shows focal averaged strong-field photoelectron spectra for a peak intensity of $I_{\text{max}} = 10^{14}$ W/cm². The remaining laser parameters correspond to the values used in the main text. We stop volume integration at the isosurface corresponding to $I_0 = 10^{13}$ W/cm², where strong-field ionization becomes negligible. Four different initial states are used, namely

(from top to bottom) symmetric initial $2p_z$, anti-symmetric initial $2p_x$ as well as “misaligned” He^+ using misalignment angles of $\alpha = 5^\circ$ and $\alpha = 10^\circ$. We observe the same suppression of the photoelectron signal in the “holographic” region for zero perpendicular final momentum for the anti-symmetric initial state, which is stable with respect to “misalignment”, c.f. Figure 2 in main text.

Figure S5(b) explores the effect of focal averaging on the “LIED” region. The top panel shows the angle-resolved strong-field photoelectron yields for the four orientations from Fig. S5(a), i.e. initial symmetric $2p_z$ (blue), anti-symmetric $2p_x$ (green) as well as results for misalignment angles of $\alpha = 5^\circ$ (red) and $\alpha = 10^\circ$ (cyan). The recollision circle is the same as in Figure 1(b) in the main text (“ $10U_p$ ” recollision circle, see also outermost circle in Fig. S5(a)). The lower panel of Fig. S5(b) shows results along the “inner” recollision circle sketched in Fig. S5(a). Again, we observe that the effects discussed in the main text for a single peak intensity of 10^{14} W/cm^2 are stable with respect to focal averaging.

Appendix D: Peak laser intensity

Figures S6 and S7 explore the robustness of the observed features as function of the peak laser intensity. Figure S6 shows strong-field photoelectron spectra for a peak intensity of $I_{\text{max}} = 2 \times 10^{14} \text{ W/cm}^2$ (left panels) and a peak intensity of $I_{\text{max}} = 3 \times 10^{14} \text{ W/cm}^2$ (right panels). Angular momentum channels up to $L \leq 80$, $|M| \leq 80$ are included for $I_{\text{max}} = 2 \times 10^{14} \text{ W/cm}^2$ and channels up to $L \leq 120$, $|M| \leq 120$ are included for $I_{\text{max}} = 3 \times 10^{14} \text{ W/cm}^2$. The remaining simulation parameters are the same as used in the main text. The same initial states from Figure S5 are used. Again, the strong-field photoelectron spectra are suppressed in the “holographic” region close to zero perpendicular final momentum ($k_\perp = 0$) for the anti-symmetric initial state, which is stable with respect to “misalignment”.

Finally, Figure S7 shows the angle-resolved photoelectron yields along the outer recollision circles shown as black lines in the photoelectron spectra for the anti-symmetric initial $2p_x$ states in Figure S6. The same color coding from Figure S5(b) is used. We observe again that the transverse structure of the returning electronic wavepacket strongly affects strong-field rescattering. The effect is robust to field misalignments with respect to the symmetry plane.

-
- [1] P. R. Bunker and P. Jensen, *Fundamentals of molecular symmetry* (Institute of Physics Publishing, 2005).
- [2] P. R. Bunker and P. Jensen, *Molecular Symmetry and Spectroscopy* (NRC Research Press, 1998).
- [3] K. J. Schafer, B. Yang, L. F. DiMauro, and K. C. Kulander, *Phys. Rev. Lett.* **70**, 1599 (1993).
- [4] P. B. Corkum, *Phys. Rev. Lett.* **71**, 1994 (1993).
- [5] F. Krausz and M. Y. Ivanov, *Rev. Mod. Phys.* **81**, 163 (2009).
- [6] C. D. Lin, A.-T. Le, Z. Chen, T. Morishita, and R. Lucchese, *J. Phys. B: At. Mol. Opt. Phys.* **43**, 122001 (2010).
- [7] T. Schultz and M. J. J. Vrakking, eds., *Attosecond and XUV spectroscopy: Ultrafast Dynamics and Spectroscopy* (Wiley, 2014).
- [8] M. Lewenstein, P. Balcou, M. Y. Ivanov, A. L’Huillier, and P. B. Corkum, *Phys. Rev. A* **49**, 2117 (1994).
- [9] O. Smirnova and M. Y. Ivanov, in *Attosecond and XUV spectroscopy: Ultrafast Dynamics and Spectroscopy*, edited by T. Schultz and M. J. J. Vrakking (Wiley, 2014) p. 201.
- [10] T. Morishita, A.-T. Le, Z. Chen, and C. D. Lin, *Phys. Rev. Lett.* **100**, 013903 (2008).
- [11] Y. Huismans, A. Rouzée, A. Gijsbertsen, J. H. Jungmann, A. S. Smolkowska, P. S. W. M. Logman, F. Lépine, C. Cauchy, S. Zamith, T. Marchenko, J. M. Bakker, G. Berden, B. Redlich, A. F. G. van der Meer, H. G. Muller, W. Vermin, K. J. Schafer, M. Spanner, M. Y. Ivanov, O. Smirnova, D. Bauer, S. V. Popruzhenko, and M. J. J. Vrakking, *Science* **331**, 61 (2011).
- [12] M. Meckel, A. Staudte, S. Patchkovskii, D. M. Villeneuve, P. B. Corkum, R. Dörner, and M. Spanner, *Nat. Phys.* **10**, 594 (2014).
- [13] S. G. Walt, B. R. Niraghatam, M. Atala, N. I. Shvetsov-Shilovski, A. von Conta, D. Baykushcheva, M. Lein, and H. J. Wörner, *Nat. Commun.* **8**, 15651 (2017).
- [14] T. Zuo, A. D. Bandrauk, and P. B. Corkum, *Chem. Phys. Lett.* **259**, 313 (1996).
- [15] M. Lein, J. P. Marangos, and P. L. Knight, *Phys. Rev. A* **66**, 051404(R) (2002).
- [16] M. Spanner, O. Smirnova, P. B. Corkum, and M. Y. Ivanov, *J. Phys. B At. Mol. Opt. Phys.* **37**, L243 (2004).
- [17] M. Meckel, D. Comtois, D. Zeidler, A. Staudte, D. Pavičić, H. C. Bandulet, H. Pépin, J. C.

- Kieffer, R. Dörner, D. M. Villeneuve, and P. B. Corkum, *Science* **320**, 1478 (2008).
- [18] C. I. Bлага, J. Xu, A. D. DiChiara, E. Sistrunk, K. Zhang, P. Agostini, T. A. Miller, L. F. DiMauro, and C. D. Lin, *Nature* **483**, 194 (2012).
- [19] J. Xu, C. I. Bлага, K. Zhang, Y. H. Lai, C. D. Lin, T. A. Miller, P. Agostini, and L. F. DiMauro, *Nat. Commun.* **5**, 4635 (2014).
- [20] M. G. Pullen, B. Wolter, A.-T. Le, M. Baudisch, M. Hemmer, A. Senftleben, C. D. Schröter, J. Ullrich, R. Moshhammer, C. D. Lin, and J. Biegert, *Nat. Commun.* **6**, 7262 (2015).
- [21] M. G. Pullen, B. Wolter, A.-T. Le, M. Baudisch, M. Scalfani, H. Pires, C. D. Schröter, J. Ullrich, R. Moshhammer, T. Pfeifer, C. D. Lin, and J. Biegert, *Nat. Commun.* **7**, 11922 (2016).
- [22] Y. Ito, C. Wang, A.-T. Le, M. Okunishi, D. Ding, C. D. Lin, and K. Ueda, *Struct. Dyn.* **3**, 034303 (2016).
- [23] B. Wolter, M. G. Pullen, A.-T. Le, M. Baudisch, K. Doblhoff-Dier, A. Senftleben, M. Hemmer, C. D. Schröter, J. Ullrich, T. Pfeifer, R. Moshhammer, S. Gräfe, O. Vendrell, C. D. Lin, and J. Biegert, *Science* **354**, 308 (2016).
- [24] O. E. Alon, V. Averbukh, and N. Moiseyev, *Phys. Rev. Lett.* **80**, 3743 (1998).
- [25] F. Schell, T. Bredtmann, C.-P. Schulz, S. Patchkovskii, M. J. J. Vrakking, and J. Mikosch, *Sci. Adv.* **4**, 8148 (2018).
- [26] S. W. Hell, *Science* **316**, 1153 (2007).
- [27] F. Morales, T. Bredtmann, and S. Patchkovskii, *J. Phys. B At. Mol. Opt. Phys.* **49**, 245001 (2016).
- [28] S. Patchkovskii and H. G. Muller, *Comput. Phys. Commun.* **199**, 153 (2016).
- [29] D. Manolopoulos, *J. Chem. Phys.* **117**, 9552 (2002).
- [30] A. M. Ermolaev, I. V. Puzynin, A. V. Selin, and S. I. Vinitzky, *Phys. Rev. A* **60**, 4831 (1999).
- [31] L. Tao and A. Scrinzi, *New J. Phys.* **14**, 013021 (2012).
- [32] M. Möller, F. Meyer, A. M. Sayler, G. G. Paulus, M. F. Kling, B. E. Schmidt, W. Becker, and D. B. Milošević, *Phys. Rev. A* **90**, 023412 (2014).
- [33] A. Becker and F. H. M. Faisal, *J. Phys. B: At. Mol. Opt. Phys.* **38**, R1 (2005).
- [34] M. Busuladžić, A. Gazibegović-Busuladžić, D. B. Milošević, and W. Becker, *Phys. Rev. A* **78**, 033412 (2008).
- [35] P. A. Korneev, S. V. Popruzhenko, S. P. Goreslavski, T.-M. Yan, D. Bauer, W. Becker,

- M. Kübel, M. F. Kling, C. Rödel, M. Wünsche, and G. G. Paulus, *Phys. Rev. Lett.* **108**, 223601 (2012).
- [36] M. Lein, N. Hay, R. Velotta, J. P. Marangos, and P. L. Knight, *Phys. Rev. Lett.* **88**, 183903 (2002).
- [37] J. Muth-Böhm, A. Becker, and F. H. M. Faisal, *Phys. Rev. Lett.* **85**, 2280 (2000).
- [38] A. F. Alharbi, A. E. Boguslavskiy, N. Thiré, G. S. Thekkadath, S. Patchkovskii, B. E. Schmidt, F. Légaré, T. Brabec, V. R. Bhardwaj, and M. Spanner, *Phys. Rev. A* **96**, 043402 (2017).
- [39] I. Barth, J. Manz, Y. Shigeta, and K. Yagi, *J. Am. Chem. Soc.* **128**, 7043 (2006).
- [40] S. Eckart, M. Kunitski, M. Richter, A. Hartung, J. Rist, F. Trinter, K. Fehre, N. Schlott, K. Henrichs, L. P. H. Schmidt, T. Jahnke, M. Schöffler, K. Liu, I. Barth, J. Kaushal, F. Morales, M. Ivanov, O. Smirnova, and R. Dörner, *Nat. Phys.* **14**, 701 (2018).
- [41] T. Bredtmann and S. Patchkovskii, in preparation.

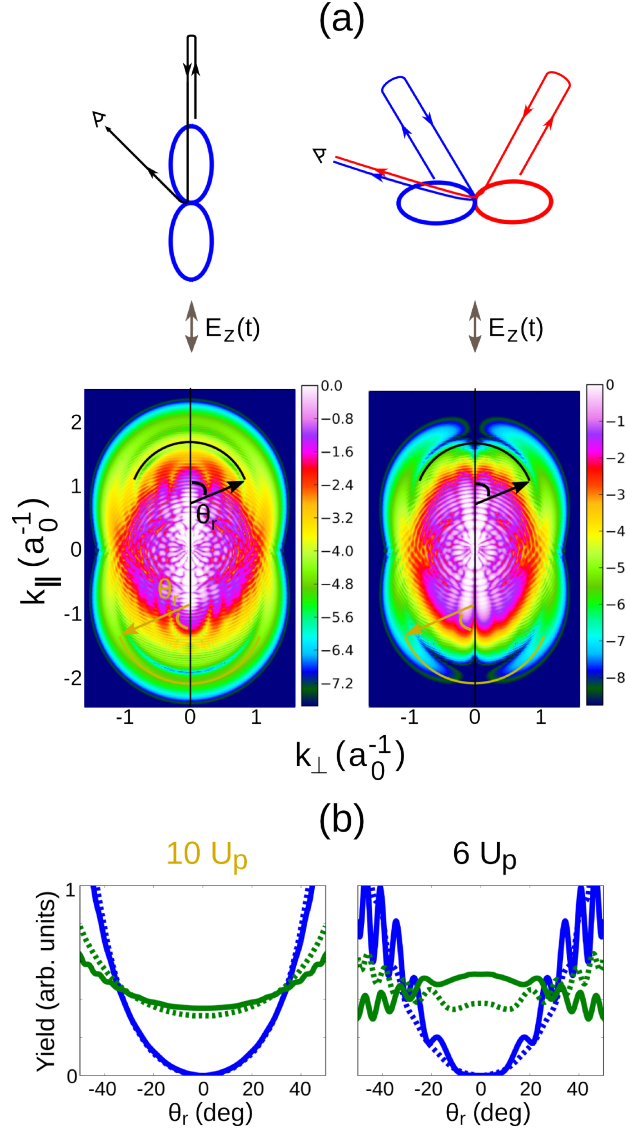


FIG. 1. (a) Angle-resolved strong-field photoelectron spectra for the He^+ ion for initial states symmetric ($|2p_z\rangle$, left) and anti-symmetric ($|2p_x\rangle$, right) with respect to the laser polarization direction. The strong (10^{14} W/cm^2) 5-cycle, 800 nm driving field is linearly polarized along the z axis. The $10U_p$ and the $6U_p$ recollision circles are indicated by the yellow (upper) and the black (lower) lines, respectively, with the definition of the deflection angle θ_r . The ionization probabilities are 0.16 ($|2p_z\rangle$) and 0.12 ($|2p_x\rangle$). The spectra are shown on a logarithmic scale. (b) Angle-resolved photoelectron yields along the two recollision circles for $|2p_z\rangle$ (green, upper lines) and $|2p_x\rangle$ (blue, lower lines). Left (right) side: yields along the $10U_p$ ($6U_p$) circle. All curves are normalized to constant area. Dashed lines: Focal-averaged yields at peak intensity of 10^{14} W/cm^2 ; see text and appendix for details.

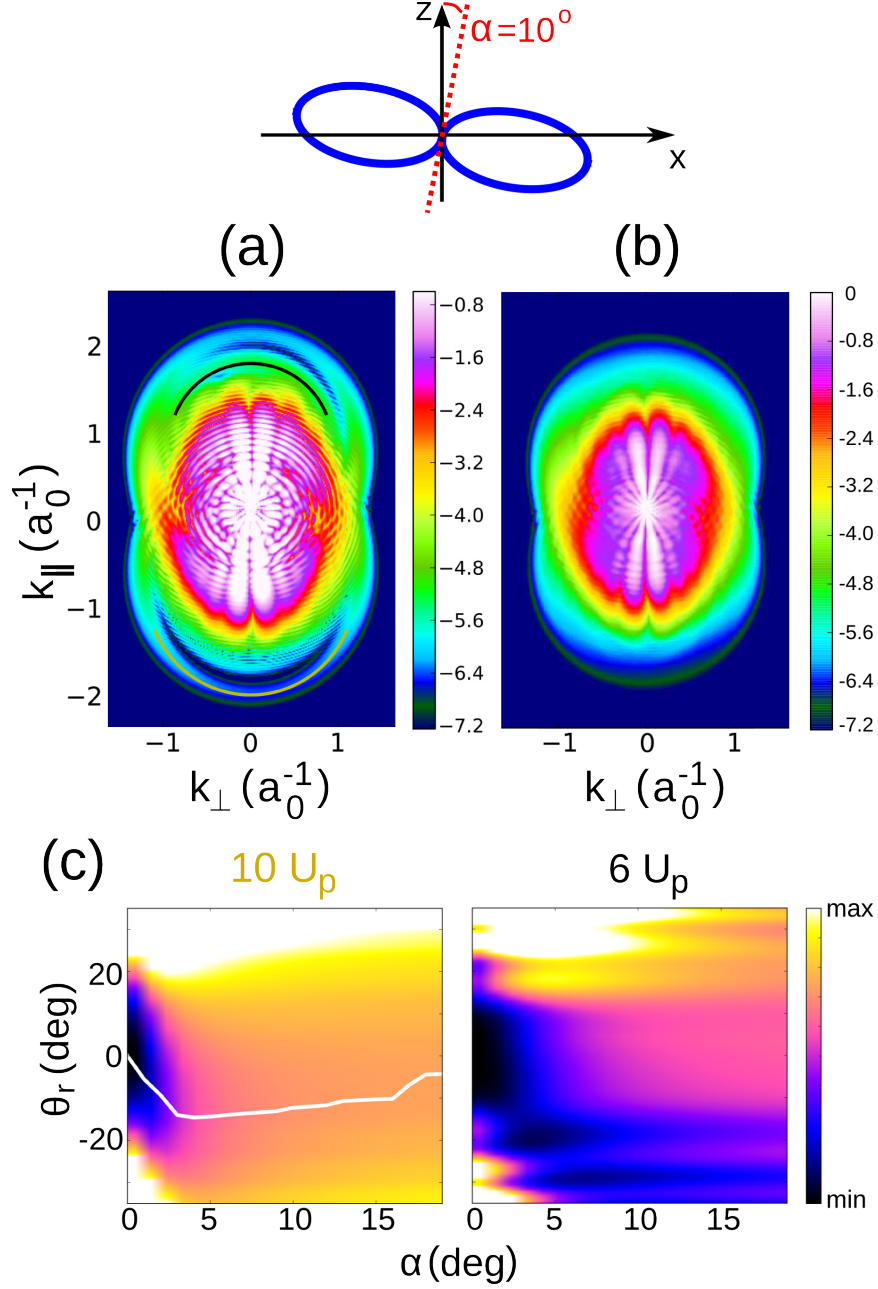


FIG. 2. (a) Strong-field photoelectron spectrum for a “misaligned” He^+ ion. The initial state $|\Psi_0\rangle$ is a $2p_x$ orbital rotated by $\alpha = 10^\circ$ around the y axis. The spectrum is shown on a logarithmic scale. (b) Same as (a), including focal-spot averaging. (c) Angle-resolved photoelectron yield along the $10U_p$ and $6U_p$ recollision circles, as function of the misalignment angle α for the single-intensity case (panel a). For the $10U_p$ circle (left), the solid line traces the minimum for each α . The yields are normalized to the same area for each α . See Fig. 1 caption for the field parameters and other definitions.

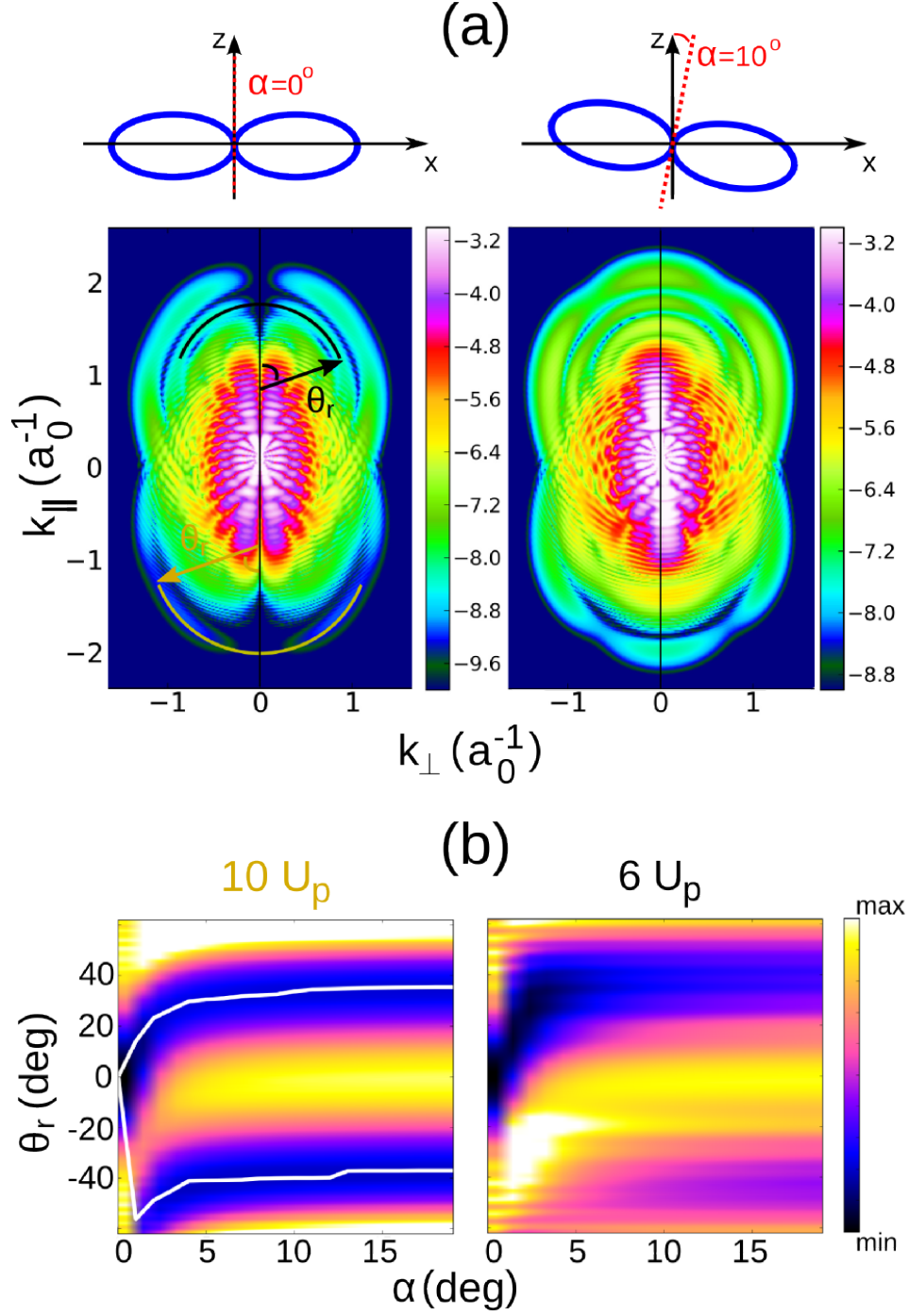


FIG. 3. (a) Strong-field photoelectron spectra for the model argon atom (see text) for two different initial states: $|\Psi_0\rangle = |3p_x\rangle$ (left) and a $3p_x$ orbital rotated by $\alpha = 10^\circ$ (right). (b) Angle-resolved photoelectron yield along the $10U_p$ and $6U_p$ recollision circles as a function of the misalignment angle α . See Fig. 1 caption for field parameters and further details.

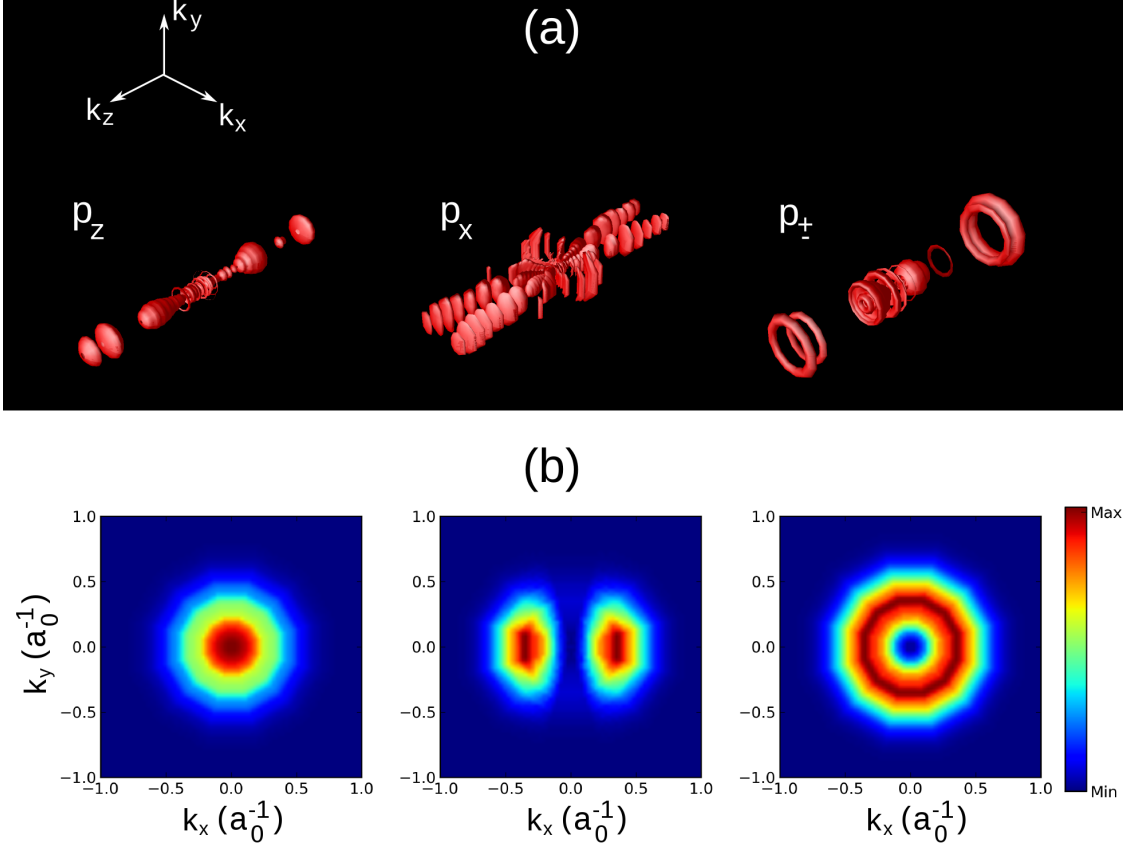


FIG. S1. (a) Isosurface plots of strong-field photoelectron spectra for the He⁺ atom with initial 2p_z (left), 2p_x (middle) and 2p_{±1} (right) states. The same linearly *z*-polarized strong-field from the main text was used. The isosurface values are 0.75 a₀³, 0.2 a₀³ and 0.75 a₀³, respectively. (b) Corresponding two-dimensional cuts in the k_xk_y-plane at k_z=2.1 a₀⁻¹.

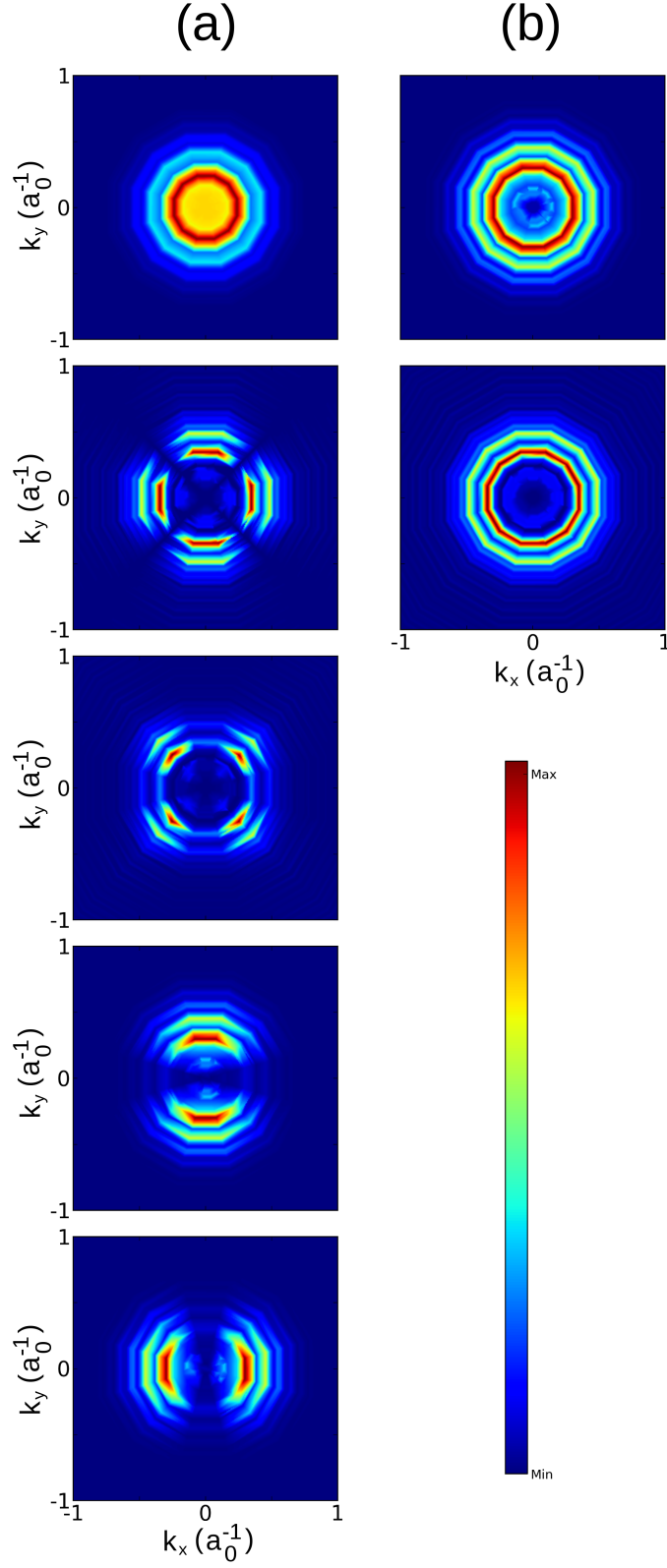


FIG. S2. Same as Figure S1(b) for the He^+ atom initially in the (from top to bottom) $3d_{z^2}$, $3d_{x^2-y^2}$, $3d_{xy}$, $3d_{yz}$, $3d_{zx}$ state (a). Panel (b) shows the corresponding results for initial $3d_{\pm 1}$ (top) and $3d_{\pm 2}$ (bottom) states.

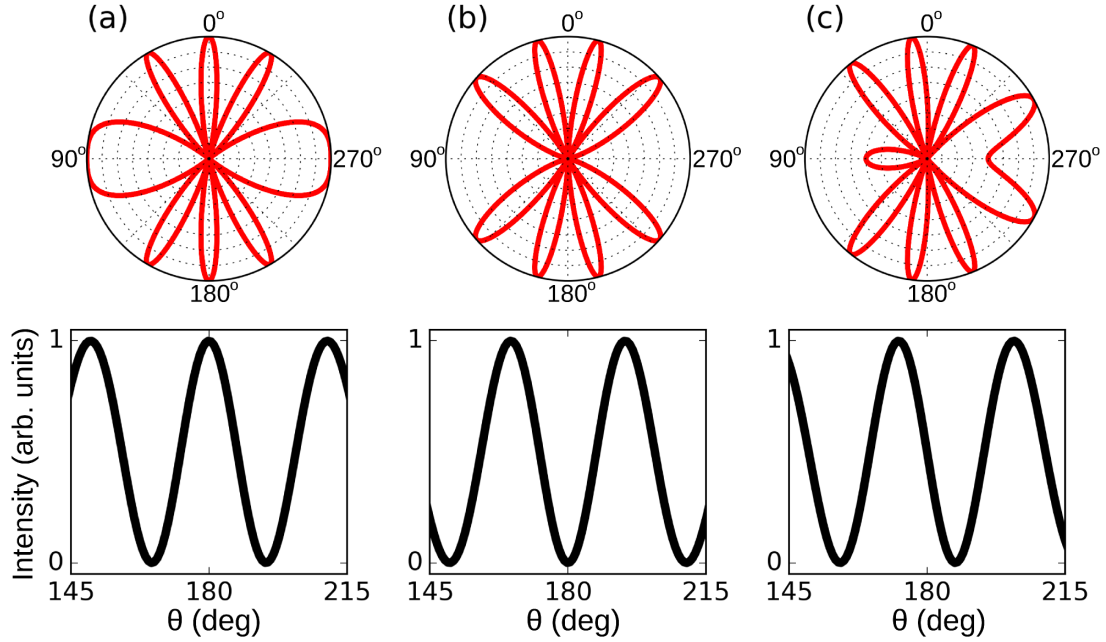


FIG. S3. Far-field double-slit diffraction pattern. The ratio of the slit separation d and the wavelength λ of the incoming beam is $d/\lambda = 2$. The phase difference Φ between the two emitters is chosen to be $\Phi = 0$ (a), $\Phi = \pi$ (b) and $\Phi = \pi/2$ (c), see text for details. The upper panels show the far-field diffraction patterns for diffraction angles $0^\circ \leq \theta \leq 360^\circ$, while the lower panels show details in the range $145^\circ \leq \theta \leq 215^\circ$.

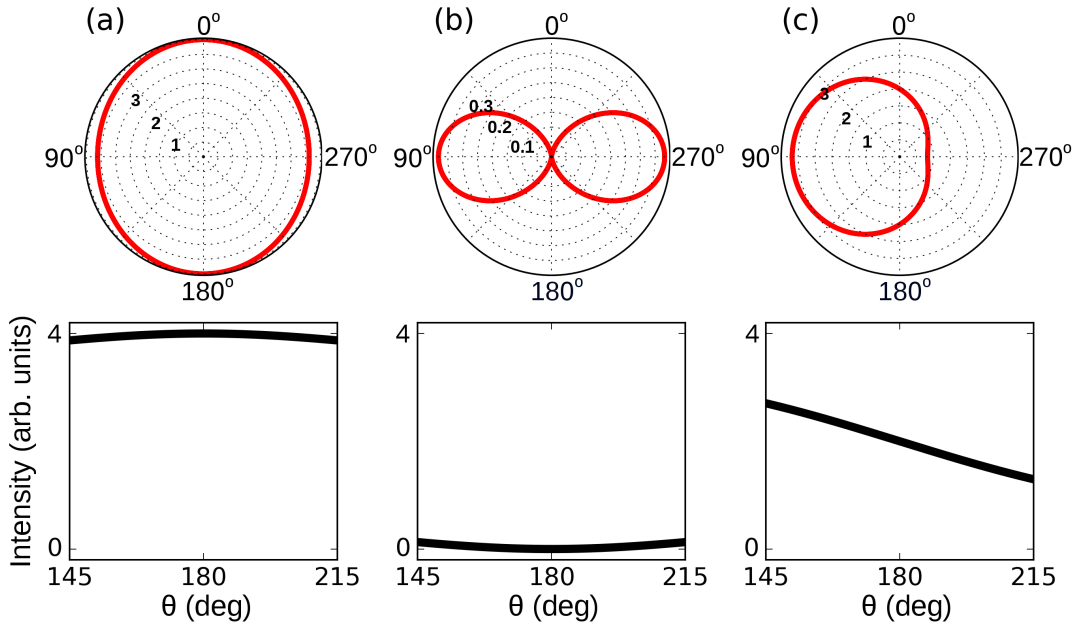


FIG. S4. Same as Figure S3 for $d/\lambda = 0.1$.

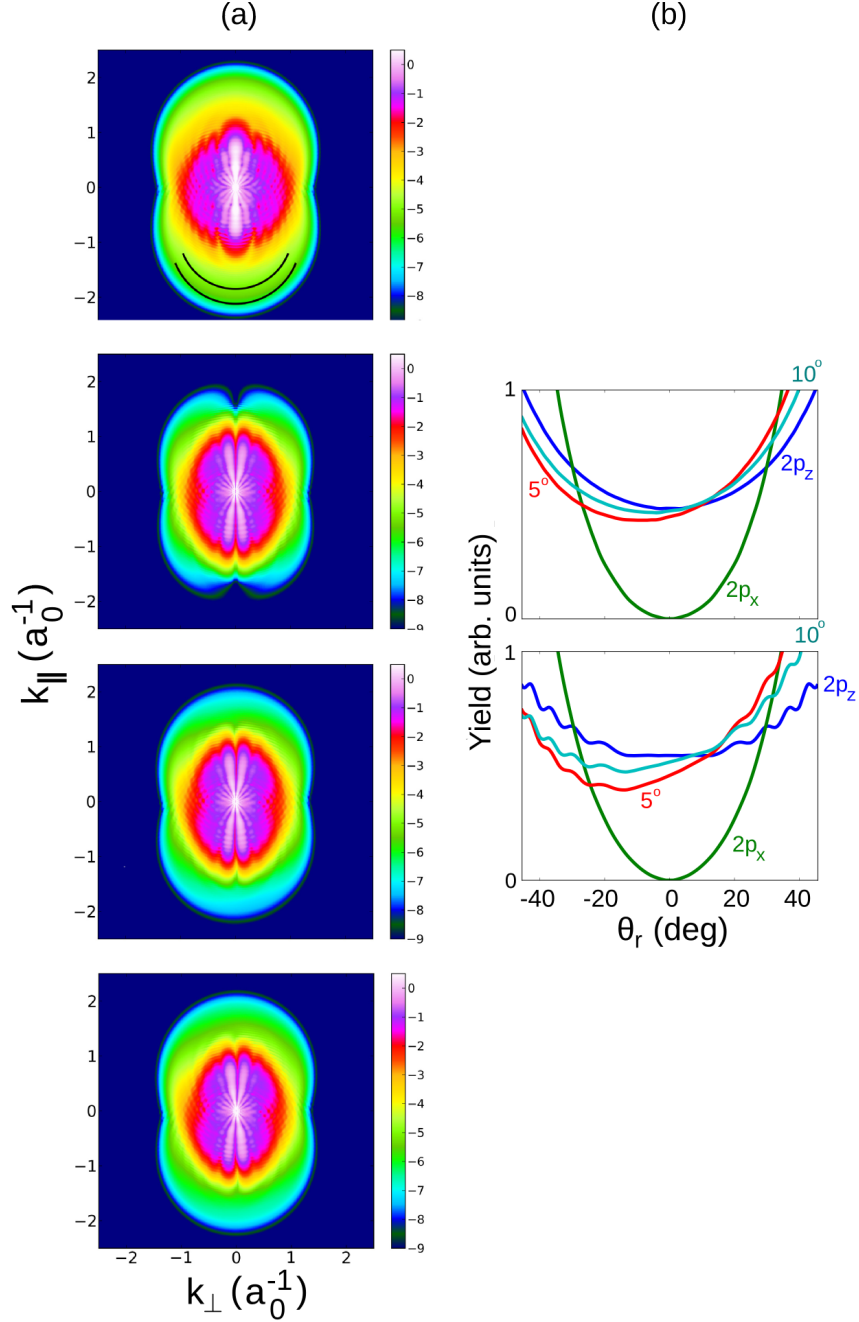


FIG. S5. (a) Focal-averaged strong-field photoelectron spectra for the He⁺ atom at the peak intensity of 10^{14} W/cm² for (from top to bottom): symmetric initial $2p_z$, anti-symmetric initial $2p_x$ as well as “misaligned” He⁺ using misalignment angles of $\alpha = 5^\circ$ and $\alpha = 10^\circ$, see main text for details. (b) Corresponding angle-resolved photoelectron yields along the 10U_p (top) and the 8U_p (bottom) recollision circles sketched in part (a) for initial $2p_z$ (blue), $2p_x$ (green) as well as $\alpha = 5^\circ$ (red) and $\alpha = 10^\circ$ (cyan), see text for further details.

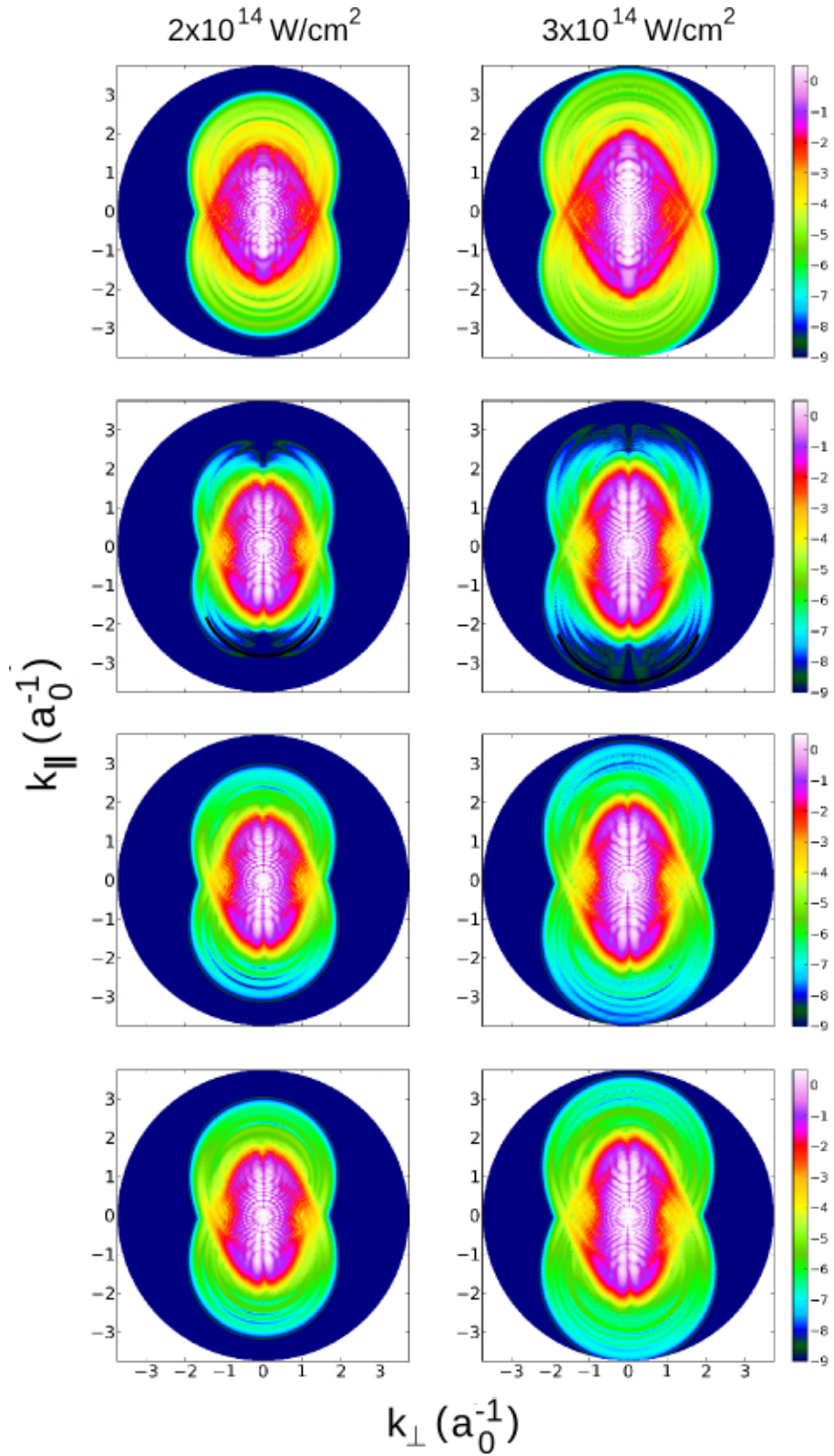


FIG. S6. Strong-field photoelectron spectra for the He⁺ atom for peak laser intensities of $I_{\text{max}} = 2 \times 10^{14} \text{ W/cm}^2$ (left) and $I_{\text{max}} = 3 \times 10^{14} \text{ W/cm}^2$ (right). The same four different initial states and remaining laser parameters as in Figure S5 are used.

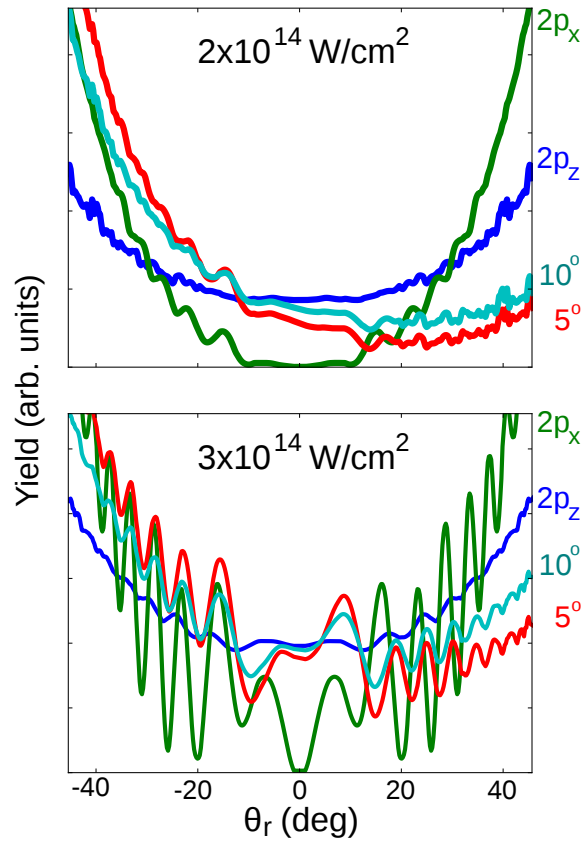


FIG. S7. Angle-resolved photoelectron yields for the He^+ atom along the outer recollision circles sketched in Fig. S6 as black lines for the four different initial states and the two peak laser intensities from Figure S6. The color coding is the same as used in Figure S5(b).